

## Binary Cu–Co catalysts derived from hydrotalcites with excellent activity and recyclability towards $\text{NH}_3\text{BH}_3$ dehydrogenation†

Cite this: *J. Mater. Chem. A*, 2013, **1**, 5370

Changming Li, Junyao Zhou, Wa Gao, Jingwen Zhao, Jie Liu, Yufei Zhao, Min Wei,\* David G. Evans and Xue Duan

The “Hydrogen economy” as an energy solution has received worldwide attention. Development of efficient, economic and recyclable catalysts for hydrogen generation from hydrogen storage materials (e.g.,  $\text{NH}_3\text{BH}_3$ , AB) under moderate conditions has been one of the most active research areas. In the well-studied transition metals, cobalt (Co) and copper (Cu) are very efficient catalysts towards  $\text{NH}_3\text{BH}_3$  dehydrogenation. In this work, we demonstrate the preparation of binary Cu–Co catalysts *via* the LDH precursor approach, which exhibit largely enhanced catalytic activity towards dehydrogenation of AB. The catalyst with a Cu/Co molar ratio of 1/1 yields a hydrolysis completion time less than 4.0 min at a rate of  $\sim 1000 \text{ mL (min}^{-1} \text{ g}_{\text{cat}})$  under the ambient conditions, comparable to the most reported noble metal catalysts (e.g., Ru, Pt). XRD,  $\text{H}_2$ -TPR, XPS and HRTEM measurements verify that the synergistic effect between highly dispersive metallic Cu and  $\text{Co}_3\text{O}_4$  species plays a key role in the significantly enhanced activity of the Cu–Co catalyst. In addition, a monolithic Cu–Co film catalyst was fabricated by an *in situ* growth-reduction method, which displays further enhanced catalytic activity, recyclability and long-term reusability. This work provides an effective strategy for the fabrication of excellent Cu–Co catalysts for  $\text{NH}_3\text{BH}_3$  decomposition, which can be used as promising candidates in pursuit of practical implementation of AB as a hydrogen storage material.

Received 29th January 2013  
Accepted 25th February 2013

DOI: 10.1039/c3ta10424a

[www.rsc.org/MaterialsA](http://www.rsc.org/MaterialsA)

### 1 Introduction

Storing hydrogen safely and efficiently is one of the major technological barriers preventing the widespread application of hydrogen-fueled cells, such as proton exchange membrane fuel cells (PEMFCs).<sup>1–3</sup> Currently, the ammonia-borane ( $\text{NH}_3\text{BH}_3$ , AB) complex has been identified as one of the leading candidates as a hydrogen reservoir owing to its low molecular weight ( $30.9 \text{ g mol}^{-1}$ ), high hydrogen content (19.6 wt%), high stability under ordinary fuel cell reaction conditions, and nontoxicity.<sup>4–8</sup> One of the major obstacles for the practical application of this system is to develop efficient, economic and recyclable catalysts for improving the kinetic and thermodynamic properties under moderate conditions.<sup>9–11</sup>

A large number of catalysts have been reported to evolve hydrogen from ammonia borane by thermal decomposition,<sup>12,13</sup> solvolysis or hydrolysis reactions.<sup>14–20</sup> To accelerate the hydrolysis reaction, the N–B bond cleavage should be facilitated by a catalyst because the  $\text{BH}_3$  formed as an intermediate would react

with a water molecule to evolve hydrogen.<sup>21</sup> Although noble metals such as Rh,<sup>22,23</sup> Ru,<sup>24,25</sup> and Pt<sup>26,27</sup> show rather good catalytic behavior for  $\text{NH}_3\text{BH}_3$  decomposition, the limited resource restricts their practical applications. Alternatively, cost-effective non-noble metals (e.g., cobalt, nickel, and iron) have also been developed.<sup>28–30</sup> However, these materials often suffer from insufficient durability/stability owing to magnetism-induced agglomeration and easy oxidation. To solve this problem, several strategies, including Co–Pd<sup>31</sup> alloy nanoparticles, Pd@Co<sup>32</sup> core–shell catalysts, and structured Co–B film<sup>33</sup> catalysts, have also been explored. Despite all this progress, a huge challenge still remains to achieve high-performance catalysts towards AB decomposition with high activity and desired durability simultaneously.

Given the problems discussed above, dispersion and stabilization of active metal species are two key factors in the design and fabrication of highly efficient catalysts for AB decomposition. Layered double hydroxides (LDHs) are a class of naturally occurring and synthetic materials generally expressed by the formula  $[\text{M}^{2+}_{1-x}\text{M}^{3+}_x(\text{OH})_2](\text{A}^{n-})_{x/n} \cdot m\text{H}_2\text{O}$ , in which  $\text{M}^{\text{II}}$  and  $\text{M}^{\text{III}}$  cations disperse in an ordered and uniform manner in brucite-like layers.<sup>34–37</sup> Recently, considerable interest has been focused on LDH materials as heterogeneous catalysts, based on their versatility in chemical composition and structural architecture.<sup>38,39</sup> Especially, a topotactic transformation of LDH

State Key Laboratory of Chemical Resource Engineering, Beijing University of Chemical Technology, Beijing 100029, P. R. China. E-mail: [weimin@mail.buct.edu.cn](mailto:weimin@mail.buct.edu.cn); Fax: +86-10-64425385; Tel: +86-10-64412131

† Electronic supplementary information (ESI) available: Additional characterization results. See DOI: 10.1039/c3ta10424a

materials into uniformly dispersed metal oxides or metal–metal oxide composites occurs on calcination in air or under reducing conditions, respectively.<sup>40–42</sup> Inspired by the structural merits of LDH materials, we explored the idea of incorporation of less active but stable Cu and highly active but less stable Co species into the LDH matrix on the atomic scale to fabricate binary Cu–Co catalysts for  $\text{NH}_3\text{BH}_3$  decomposition. The resulting catalysts would possess the following desirable features: firstly, the high dispersion of Cu and Co species facilitates a synergistic effect for the improvement of catalytic activity; secondly, the presence of LDH matrix inhibits the agglomeration of active components and thus enhances the long-term stability.

In this work, we report the fabrication of binary Cu–Co powdered catalysts *via* a facile two-step procedure involving preparation of a ternary CuCoAl-LDH precursor followed by a calcination–reduction process, and demonstrate its application as an efficient catalyst for hydrogen generation from  $\text{NH}_3\text{BH}_3$  decomposition. Based on the synergistic effect between highly dispersive Cu and Co species, the catalyst (Cu/Co = 1/1, molar ratio) yields largely enhanced catalytic activity with a hydrolysis completion time less than 4.0 min at a rate of  $\sim 1000 \text{ mL} (\text{min}^{-1} g_{\text{cat}})$  under the ambient conditions, which is comparable to the most reported noble metal catalysts (*e.g.*, Ru, Pt). XRD,  $\text{H}_2$ -TPR, HRTEM and XPS measurements demonstrate that the uniform interspersions between metallic Cu and  $\text{Co}_3\text{O}_4$  nanoparticles maximizes the synergistic effect, accounting for the significantly enhanced activity of the Cu–Co catalyst. Moreover, we have successfully fabricated a monolithic highly dispersed Cu–Co film catalyst by an *in situ* growth-reduction method, which exhibits further enhanced catalytic performance with the complete decomposition of  $\text{NH}_3\text{BH}_3$  within 3.0 min as well as long-term reusability without obvious activity loss.

## 2 Experimental section

### 2.1 Materials

The pure aluminum substrate (purity >99.99%; thickness 0.2 mm) was purchased from Beijing General Research Institute for Non-Ferrous Metals. Ammonia borane complex ( $\text{NH}_3\text{BH}_3$ , AB, 97%) was purchased from Sigma Aldrich and used as received. The following analytical grade chemicals were used without further purification: NaOH,  $\text{Na}_2\text{CO}_3$ ,  $\text{Cu}(\text{NO}_3)_2 \cdot 3\text{H}_2\text{O}$ ,  $\text{Co}(\text{NO}_3)_2 \cdot 6\text{H}_2\text{O}$ , and  $\text{Al}(\text{NO}_3)_3 \cdot 9\text{H}_2\text{O}$ . Deionized water was used in all the experimental processes.

### 2.2 Fabrication of the Cu–Co catalysts

**Synthesis of powdered catalysts.** Powdered  $(\text{Cu}_x\text{Co}_y)_2\text{Al-LDHs}$  ( $([\text{Cu}^{2+}] + [\text{Co}^{2+}])/[\text{Al}^{3+}] = 2/1$ ) with tunable compositions ( $x/y$ ) were synthesized by a co-precipitation method. Typically,  $\text{Cu}(\text{NO}_3)_2 \cdot 3\text{H}_2\text{O}$ ,  $\text{Co}(\text{NO}_3)_2 \cdot 6\text{H}_2\text{O}$  and  $\text{Al}(\text{NO}_3)_3 \cdot 9\text{H}_2\text{O}$  with a  $(\text{Cu}^{2+} + \text{Co}^{2+})/\text{Al}^{3+}$  molar ratio of 2.0 were dissolved in 250 mL of deionized water to give a solution with a total cationic concentration of 0.3 M (Solution A). NaOH (2 M) and  $\text{Na}_2\text{CO}_3$  (1 M) were dissolved together to obtain a 100 mL of base solution (Solution B). Solution B was then added dropwise to Solution A under vigorous stirring until the pH value reached to

10.0. The resulting suspension was aged in a water bath at 75 °C with stirring for 24 h. The obtained precipitation was washed thoroughly with water and dried in an oven at 60 °C overnight. The LDH precursor was subsequently calcinated at 500 °C for 4 h (denoted as  $(\text{Cu}_x\text{Co}_y)_2\text{Al-MMO}$ ) and then reduced at 300 °C for 3 h in a hydrogen atmosphere (denoted as  $(\text{Cu}_x\text{Co}_y)_2\text{Al-Cat}$ ).

**Fabrication of the monolithic Cu–Co film catalyst.** The CuCoAl-LDH/Al films were prepared by *in situ* crystallization on the pure aluminum substrate. The substrate was cleaned with acetone, ethanol and deionized water in sequence before use. In a typical procedure,  $\text{Cu}(\text{NO}_3)_2 \cdot 3\text{H}_2\text{O}$  (0.016 mol),  $\text{Co}(\text{NO}_3)_2 \cdot 6\text{H}_2\text{O}$  (0.016 mol) and  $(\text{NH}_2)_2\text{CO}$  (0.194 mol) were dissolved in deionized water to form a clear solution with a total volume of 600 mL. The Al substrate (28 cm × 15 cm) was rolled into a tubular shape and immersed vertically in the solution, which was heated at 75 °C for 24 h. Afterwards, the substrate was withdrawn, rinsed with deionized water and dried at room temperature. The as-prepared CuCoAl-LDH film was heated at 500 °C for 4 h, and then cooled to room temperature to obtain the CuCoAl-MMO film. The sample was reduced with  $\text{H}_2$  at 300 °C for 3 h before catalytic tests.

### 2.3 Catalytic evaluation towards hydrogen generation from $\text{NH}_3\text{BH}_3$ decomposition

The catalytic activity of the catalysts toward hydrolysis of AB was determined by measuring the rate of hydrogen. The scheme of the experimental setup is shown in Fig. S1.† The catalyst was immersed into a solution of AB (50 mM, 20 mL). The generated hydrogen volume was measured through a gas volumetric method in an appropriate reaction chamber with a thermostatic bath, wherein the temperature was kept constant.<sup>28</sup> In all the runs, the catalyst was placed on the insertion device (PVC circular disc with a rod) inside the reaction chamber; the reaction system was sealed and stirred at 800 rpm at 298 K.

### 2.4 Characterization

Hydrogen temperature programmed reduction ( $\text{H}_2$ -TPR) was conducted in a quartz tube reactor on a Micromeritics Chemisorb 2720 with a thermal conductivity detector (TCD). In each case, 100 mg of sample was sealed in the reactor, and then a gaseous mixture of  $\text{H}_2$  and Ar (1 : 9, v/v) was fed to the reactor at  $40 \text{ mL min}^{-1}$ . The temperature was raised to 800 °C at a heating rate of  $10 \text{ }^\circ\text{C min}^{-1}$ . Powder XRD measurements were performed on a Rigaku XRD-6000 diffractometer, using Cu K $\alpha$  radiation ( $\lambda = 0.15418 \text{ nm}$ ) at 40 kV, 40 mA, with a scanning rate of  $10^\circ \text{ min}^{-1}$ , and a  $2\theta$  angle ranging from  $3^\circ$  to  $90^\circ$ . X-ray photoelectron spectra (XPS) were recorded on a Thermo VG Escalab 250 X-ray photoelectron spectrometer at a pressure of  $\sim 2 \times 10^{-9} \text{ Pa}$  with Al K $\alpha$  X-rays as the excitation source. The element content in the samples was determined by ICP-AES (Shimadzu ICPS-7500). The morphology of the samples was investigated using a Zeiss Supra 55 scanning electron microscope (SEM) with an accelerating voltage of 20 kV, combined with energy dispersive X-ray spectroscopy (EDS) for the determination of metal composition. Transmission electron microscopy (TEM) images were recorded with JEOL JEM-2010

high resolution transmission electron microscopes. The accelerating voltage was 200 kV.

### 3 Results and discussion

#### 3.1 Structural and morphological studies of the powdered catalysts

The  $(\text{Cu}_x\text{Co}_y)_2\text{Al-LDH}$  precursors were successfully prepared by the co-precipitation method. Fig. 1 shows XRD patterns of the  $(\text{Cu}_x\text{Co}_y)_2\text{Al-LDH}$ s with various Cu/Co ratios, all of which can be indexed as a rhombohedral structure with the typical (003) and (006) reflections at  $\sim 12^\circ$  and  $24^\circ$  for LDH materials, respectively. No other crystalline phase was detected, indicating the high purity of these LDH materials. The initial and the resulting metal ratios of the products determined by inductively coupled plasma emission spectroscopy (ICP-AES) are also summarized in Table 1. The nominal ratio of the total divalent to trivalent metal was maintained to be 2 : 1, and it can be seen that the metal ratios in these products are rather close to that in the feed element. After calcination at  $500^\circ\text{C}$ , the  $(\text{Cu}_x\text{Co}_y)_2\text{Al-LDH}$  precursors transformed into mixed metal oxides (denoted as  $(\text{Cu}_x\text{Co}_y)_2\text{Al-MMO}$ ), as shown in Fig. S2.† For the  $\text{Cu}_2\text{Al-MMO}$  sample, only CuO crystalline phase with typical (002) and (111)

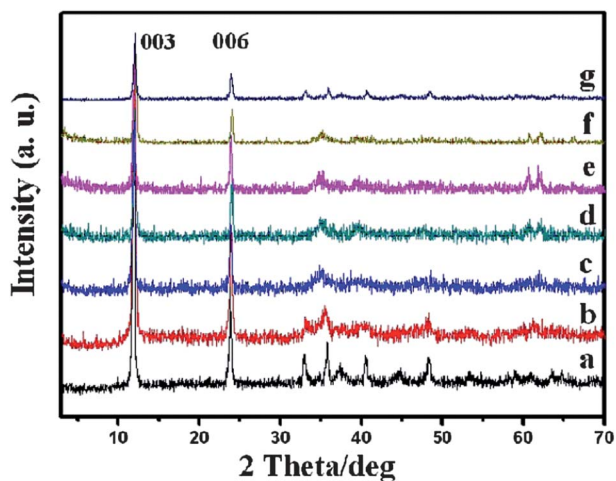


Fig. 1 XRD patterns of the as-synthesized  $(\text{Cu}_x\text{Co}_y)_2\text{Al-LDH}$ s with various ratios of  $x(\text{Cu}) : y(\text{Co})$ : (a) 1 : 0, (b) 0.87 : 0.13, (c) 0.75 : 0.25, (d) 0.50 : 0.50, (e) 0.25 : 0.75, (f) 0.13 : 0.87, and (g) 0 : 1.

Table 1 Nominal and determined metal ratios for the synthesized  $(\text{Cu}_x\text{Co}_y)_2\text{Al-LDH}$  precursors

| Samples   | Nominal ratio<br>( $\text{Cu}^{2+}/\text{Co}^{2+}/\text{Al}^{3+}$ ) | Determined ratio<br>( $\text{Cu}^{2+}/\text{Co}^{2+}/\text{Al}^{3+}$ ) |
|---|---|--|
| $\text{Cu}_2\text{Al-LDH}$ s                          | 2.00/0.00/1.00  | 1.98/0.00/1.02   |
| $(\text{Cu}_{0.87}\text{Co}_{0.13})_2\text{Al-LDH}$ s | 1.75/0.25/1.00  | 1.72/0.26/0.98   |
| $(\text{Cu}_{0.75}\text{Co}_{0.25})_2\text{Al-LDH}$ s | 1.50/0.50/1.00  | 1.45/0.47/0.95   |
| $(\text{Cu}_{0.50}\text{Co}_{0.50})_2\text{Al-LDH}$ s | 1.00/1.00/1.00  | 0.94/0.98/0.95   |
| $(\text{Cu}_{0.25}\text{Co}_{0.75})_2\text{Al-LDH}$ s | 0.50/1.50/1.00  | 0.45/1.48/0.96   |
| $(\text{Cu}_{0.13}\text{Co}_{0.87})_2\text{Al-LDH}$ s | 0.25/1.75/1.00  | 0.24/1.70/1.03   |
| $\text{Co}_2\text{Al-LDH}$ s                          | 0.00/2.00/1.00  | 0.00/1.97/1.05   |

reflections at  $\sim 35.8^\circ$  and  $38.9^\circ$  (JCPDS 89-5899) was observed (Fig. S2a†), respectively. The broadened half-peak-width indicates a small size of the CuO nanoparticles. As Co is introduced with a gradually increased content, the intensity of CuO phase decreases, while a spinel phase (mainly  $\text{Co}_3\text{O}_4$ )<sup>43</sup> appears (JCPDS 78-1970:  $\sim 31.5^\circ$ ,  $37^\circ$ ,  $45^\circ$ , and  $65.7^\circ$  assigned to (220), (311), (400), and (440) reflections) with increasingly enhanced intensity (Fig. S2b–f†). Finally a pure spinel phase is obtained in the  $\text{Co}_2\text{Al-MMO}$  sample (Fig. S2g†).

Fig. 2 shows the XRD patterns for the catalysts obtained by reduction of  $(\text{Cu}_x\text{Co}_y)_2\text{Al-MMO}$  samples at an assigned temperature of  $300^\circ\text{C}$  (denoted as  $(\text{Cu}_x\text{Co}_y)_2\text{Al-Cat}$ ). For the sample of  $\text{Cu}_2\text{Al-Cat}$ , metal Cu species with (111) and (200) reflections at  $2\theta$  of  $43.4^\circ$  and  $50.5^\circ$  (JCPDS 85-1326) were observed, indicating the transformation of CuO to metallic Cu during the reduction process. With the increase of Co content, from Fig. 2a–g, the reflection intensity of metallic Cu decreases gradually, accompanied by the enhanced reflection intensity of the spinel phase ( $\text{Co}_3\text{O}_4$ ). The hydrogen temperature programmed reaction ( $\text{H}_2\text{-TPR}$ ) measurements were carried out to provide information on the redox properties of three typical MMO samples:  $\text{Cu}_2\text{Al-MMO}$ ,  $(\text{Cu}_{0.50}\text{Co}_{0.50})_2\text{Al-MMO}$ , and  $\text{Co}_2\text{Al-MMO}$  (Fig. 3). The sample of  $\text{Cu}_2\text{Al-MMO}$  (Fig. 3, curve a) exhibits a main peak at  $197^\circ\text{C}$ , which is attributed to the reduction of CuO to metal Cu. The Co-incorporated counterpart ( $\text{Cu}_{0.50}\text{Co}_{0.50})_2\text{Al-MMO}$  (Fig. 3, curve b) displays a strong peak at  $223^\circ\text{C}$ , which is also assigned to reduction of copper oxide. The increased reduction temperature compared with  $\text{Cu}_2\text{Al-MMO}$  is due to the interaction between cobalt–copper mixed oxides.<sup>44</sup> The subsequent two broad peaks at  $361^\circ\text{C}$  and  $478^\circ\text{C}$  can be attributed to the reduction of  $\text{Co}_3\text{O}_4$  in two steps ( $\text{Co}_3\text{O}_4 \rightarrow \text{CoO} \rightarrow \text{Co}$ ).<sup>43</sup> In the case of the  $\text{Co}_2\text{Al-MMO}$  sample (Fig. 3, curve c), the peaks at  $360^\circ\text{C}$  and  $510^\circ\text{C}$  are also observed, corresponding to the reduction of the  $\text{Co}_3\text{O}_4$  phase. The remarkably higher peak at  $630^\circ\text{C}$  is possibly attributed to the reduction of the Al-contained spinel phase (e.g.,  $\text{CoAl}_2\text{O}_4$ ).<sup>43</sup> The TPR results demonstrate the formation of metal Cu and residual  $\text{Co}_3\text{O}_4$  phases in

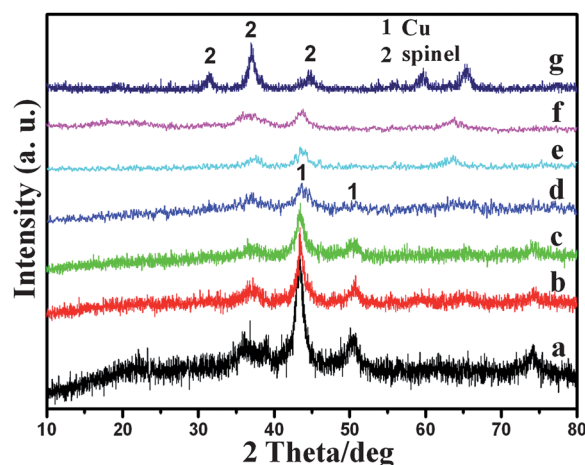
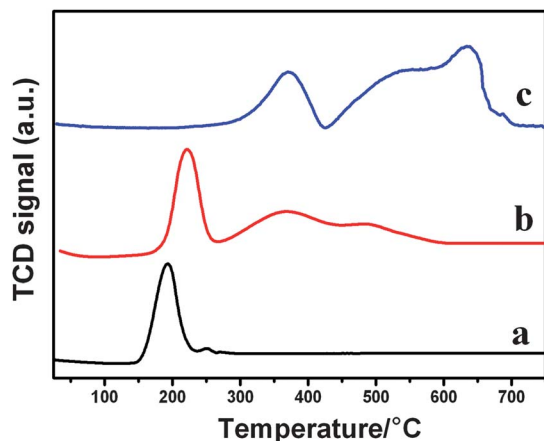


Fig. 2 XRD patterns of the  $(\text{Cu}_x\text{Co}_y)_2\text{Al-Cat}$  samples with various ratios of  $x(\text{Cu}) : y(\text{Co})$ : (a) 1 : 0, (b) 0.87 : 0.13, (c) 0.75 : 0.25, (d) 0.50 : 0.50, (e) 0.25 : 0.75, (f) 0.13 : 0.87, and (g) 0 : 1.

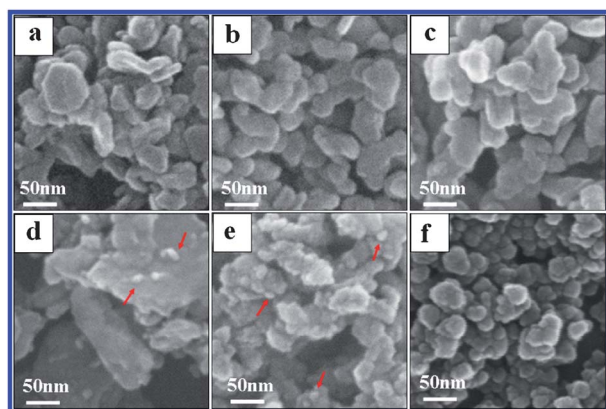


**Fig. 3** H<sub>2</sub>-TPR profiles of (a) Cu<sub>2</sub>Al-MMO, (b) (Cu<sub>0.50</sub>Co<sub>0.50</sub>)<sub>2</sub>Al-MMO, and (c) Co<sub>2</sub>Al-MMO.

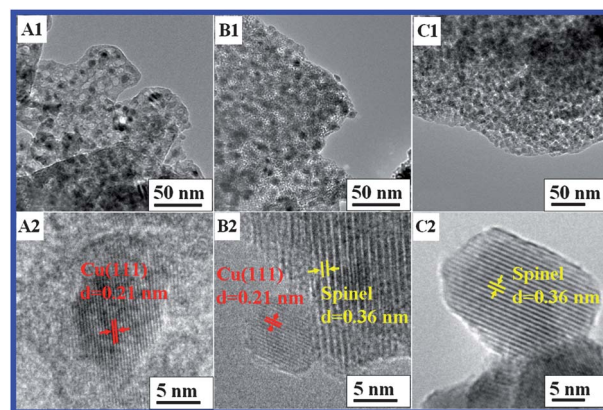
the (Cu<sub>x</sub>Co<sub>y</sub>)<sub>2</sub>Al-Cat samples, which is in good agreement with the XRD patterns (Fig. 2).

Fig. 4 shows the SEM images of the LDH precursors and the corresponding catalysts after calcination and reduction processes. The LDH precursors (Fig. 4a–c) display smooth and uniform nanocrystals with diameter of 30–100 nm. Calcination of the LDH samples leads to its transformation into MMO, which maintains the original morphology of LDH precursors (Fig. S3†). After reduction of MMO samples in hydrogen at 300 °C, numerous tiny particles (metallic Cu species) attaching to the matrix are observed (shown by the red arrows in Fig. 4d and e) in the Cu<sub>2</sub>Al-Cat and (Cu<sub>0.50</sub>Co<sub>0.50</sub>)<sub>2</sub>Al-Cat samples. However, this is absent in the case of the Co<sub>2</sub>Al-Cat sample (Fig. 4f), except for a little shrink in the particle size compared with its LDH precursor.

The structure of the catalysts was further investigated by TEM (Fig. 5). For the sample of Cu<sub>2</sub>Al-Cat (Fig. 5A1), highly dispersed nanoparticles with diameter of 3–10 nm are distributed in the amorphous Al<sub>2</sub>O<sub>3</sub> matrix, and the fringes with a



**Fig. 4** SEM images of the LDH precursors and the resulting catalysts: (a) Cu<sub>2</sub>Al-LDHs, (b) (Cu<sub>0.50</sub>Co<sub>0.50</sub>)<sub>2</sub>Al-LDHs, (c) Co<sub>2</sub>Al-LDHs, (d) Cu<sub>2</sub>Al-Cat, (e) (Cu<sub>0.50</sub>Co<sub>0.50</sub>)<sub>2</sub>Al-Cat, and (f) Co<sub>2</sub>Al-Cat. Tiny Cu nanoparticles can be seen as shown by the red arrows.



**Fig. 5** TEM images of the catalysts: (A1) Cu<sub>2</sub>Al-Cat, (B1) (Cu<sub>0.50</sub>Co<sub>0.50</sub>)<sub>2</sub>Al-Cat, and (C1) Co<sub>2</sub>Al-Cat with the corresponding HRTEM images in A2, B2, and C2, respectively.

lattice spacing of 0.21 nm can be indexed to the (111) plane of a face-centered cubic Cu (Fig. 5A2). This further confirms the reduction of CuO to Cu nanoparticles at 300 °C in a H<sub>2</sub> atmosphere. As the Co element is introduced in the case of the (Cu<sub>0.50</sub>Co<sub>0.50</sub>)<sub>2</sub>Al-Cat sample, the phase composition of this sample is rather complex (Fig. 5B1). Both a metal Cu phase and a spinel phase Co<sub>3</sub>O<sub>4</sub> with lattice spacings of 0.21 nm and 0.36 nm were identified, respectively, and Cu nanoparticles were immobilized on the surface of spinel (Fig. 5B2). In the case of the Co<sub>2</sub>Al-Cat sample, numerous small grains (~10 nm) with serious agglomeration were observed (Fig. 5C1), which are identified as the spinel phase Co<sub>3</sub>O<sub>4</sub> (Fig. 5C2). No lattice spacings assigned to the Co or CoO phase were observed. Based on the results of XRD, TPR and TEM, it is concluded that the Cu and Co species exist as a metal and a spinel phase in the (Cu<sub>x</sub>Co<sub>y</sub>)<sub>2</sub>Al-Cat samples, respectively.

### 3.2 The catalytic performance of powdered catalysts towards NH<sub>3</sub>BH<sub>3</sub> hydrolysis

To study the catalytic behavior, the as-synthesized (Cu<sub>x</sub>Co<sub>y</sub>)<sub>2</sub>Al-Cat samples were dispersed in AB aqueous solution respectively at room temperature under a fixed magnetic stirring. Fig. 6 shows the plots of generated H<sub>2</sub> versus time for the AB solution (20 mL, 50 mM) in the presence of (Cu<sub>x</sub>Co<sub>y</sub>)<sub>2</sub>Al-Cat sample (20 mg). From these curves, 3 mmol of H<sub>2</sub> (~74 mL) is generated based on the complete decomposition of 1 mmol of AB complex, indicating a full hydrolysis of the AB complex. Therefore, the catalytic activity can be characterized by the reaction time of a completed hydrolysis. It can be observed that the Co<sub>2</sub>Al-Cat sample is almost inert for AB hydrolysis. With the increase of Cu/Co ratio from 0/1 to 1/1, the catalytic activity for NH<sub>3</sub>BH<sub>3</sub> hydrolysis enhances significantly. However, a further increase of Cu/Co ratio from 1/1 to 1/0 leads to the decrease of catalytic activity. The (Cu<sub>0.50</sub>Co<sub>0.50</sub>)<sub>2</sub>Al-Cat exhibits the highest activity towards AB hydrolysis reaction with a hydrolysis completion time less than 4.0 min at a rate of ~1000 mL (min<sup>-1</sup> g<sub>cat</sub>), which is comparable to the noble metal Ru or Pt catalyst reported previously.<sup>10</sup> The largely improved catalytic activity of

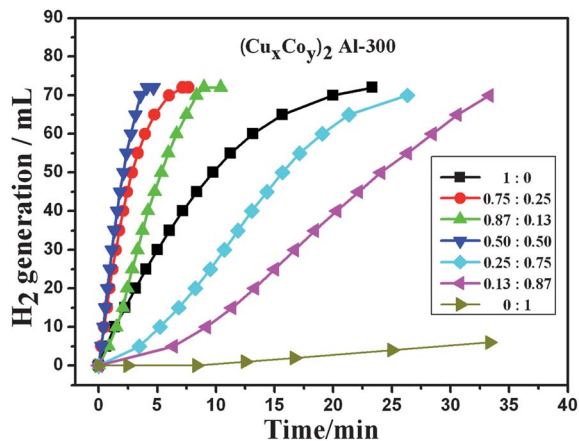


Fig. 6 Plot of H<sub>2</sub> volume vs. time in the presence of (Cu<sub>x</sub>Co<sub>y</sub>)<sub>2</sub>Al-Cat with various Cu/Co ratios ( $w_{\text{cat}} = 20$  mg, [AB] = 50 mM, (Cu + Co)/AB = 0.09, and  $T = 25 \pm 1$  °C).

the binary Cu–Co catalysts compared with their single metal counterparts indicates a synergistic effect between the binary components. The influence of reduction temperature for (Cu<sub>0.50</sub>Co<sub>0.50</sub>)<sub>2</sub>Al-Cat (in the range of 300–600 °C) on the catalytic performance towards AB hydrolysis is demonstrated in Fig. S4,† from which the activity decreases with the increase of reduction temperature. The reduced half-peak-width in the XRD reflection of the metal Cu phase from 300 to 600 °C indicates the agglomeration of Cu nanoparticles (Fig. S5†), which is most probably responsible for the loss of catalytic activity of (Cu<sub>0.50</sub>Co<sub>0.50</sub>)<sub>2</sub>Al-Cat obtained at higher reduction temperature. The reusability of the best powdered catalyst (Cu<sub>0.50</sub>Co<sub>0.50</sub>)<sub>2</sub>Al-Cat was also evaluated (Fig. S6†). An obvious decrease in activity towards NH<sub>3</sub>BH<sub>3</sub> dehydrogenation was observed in three consecutive cycles, mainly suffering from the weight loss of the powdered catalyst during the separation process.

To obtain further insights into the structure–function correlations, X-ray photoelectron spectra (XPS) were obtained for the samples of (Cu<sub>0.50</sub>Co<sub>0.50</sub>)<sub>2</sub>Al-Cat and Co<sub>2</sub>Al-Cat before and after the catalytic reaction. The survey spectra for Cu 2p, Co 2p, and B 1s are displayed in Fig. 7, all of which are referenced to the residual carbon at a binding energy (BE) of 284.6 eV. For the sample of fresh (Cu<sub>0.50</sub>Co<sub>0.50</sub>)<sub>2</sub>Al-Cat, the peaks at 932.5 eV and 952.3 eV (Fig. 7A, curve a) are attributed to Cu 2p of metal Cu;<sup>45,46</sup> peaks at 781.3 eV and 797.2 eV (Fig. 7B, curve a) correspond to Co 2p of Co<sub>3</sub>O<sub>4</sub>,<sup>47</sup> respectively. This further confirmed the presence of metal Cu and spinel phase Co<sub>3</sub>O<sub>4</sub> in the fresh (Cu<sub>0.50</sub>Co<sub>0.50</sub>)<sub>2</sub>Al-Cat. No obvious change in Cu 2p for the used catalyst can be observed (Fig. 7A, curve b). It is worth noting that a new Co 2p XPS peak at 778.1 eV for the used catalyst is clearly observed (Fig. 7B, curve b), which can be assigned to metallic Co species. However, it is not the case in the used Co<sub>2</sub>Al-Cat (Fig. 7C, curve b) compared with its fresh form (Fig. 7C, curve a), suggesting that the existence of metal Cu species induces partial reduction of Co<sub>3</sub>O<sub>4</sub> to metal Co during the reaction process in the case of (Cu<sub>0.50</sub>Co<sub>0.50</sub>)<sub>2</sub>Al-Cat. Additionally, the used (Cu<sub>0.50</sub>Co<sub>0.50</sub>)<sub>2</sub>Al-Cat shows no residual boron element (Fig. 7D), indicating the absence of Co–B. It is well known that metal Co is more active in AB hydrolysis than metal Cu;<sup>10</sup>

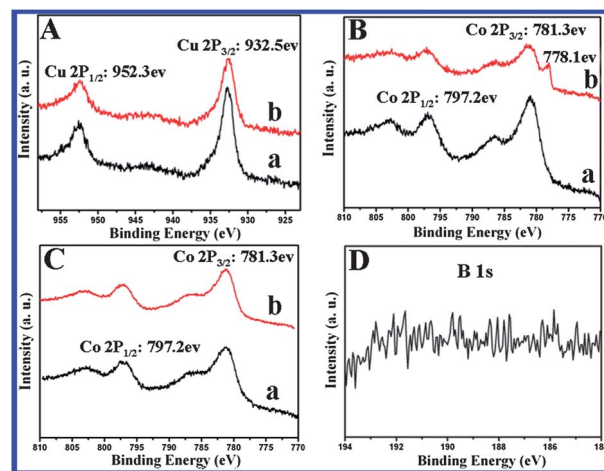


Fig. 7 XPS spectra of (A) Cu 2p, (B) Co 2p of the (Cu<sub>0.50</sub>Co<sub>0.50</sub>)<sub>2</sub>Al-Cat sample, and (C) Co 2p of the Co<sub>2</sub>Al-Cat sample: (a) the fresh catalyst; (b) the used catalyst. (D) XPS spectrum of B 1s of the used (Cu<sub>0.50</sub>Co<sub>0.50</sub>)<sub>2</sub>Al-Cat.

therefore, it is very significant for observing the metallic Co species in the used (Cu<sub>0.50</sub>Co<sub>0.50</sub>)<sub>2</sub>Al-Cat sample.

TEM and XPS results above confirm that Cu and Co species in the fresh (Cu<sub>x</sub>Co<sub>y</sub>)<sub>2</sub>Al-Cat samples are present as the metal Cu and spinel phase Co<sub>3</sub>O<sub>4</sub>, respectively; the catalytic behavior indicates that the metal Cu species plays a key role in AB hydrolysis, other than the spinel phase, which is consistent with the previous reports.<sup>47</sup> However, significantly enhanced catalytic activity was observed for the (Cu<sub>0.50</sub>Co<sub>0.50</sub>)<sub>2</sub>Al-Cat, and the existence of much Cu or Co is unfavourable for catalytic performance. The XPS spectra further verify that the interaction of the Cu–Co species in the (Cu<sub>0.50</sub>Co<sub>0.50</sub>)<sub>2</sub>Al-Cat facilitates the generation of highly active metal Co species, which is responsible for the enhanced catalytic performance of Cu–Co binary catalysts for AB hydrolysis. Therefore, it is concluded that the interspersed and synergistic effects of the binary Cu–Co species in the (Cu<sub>0.50</sub>Co<sub>0.50</sub>)<sub>2</sub>Al-Cat are the key factors for its excellent catalytic behavior.

### 3.3 The structure and catalytic performance of the monolithic Cu–Co film catalyst

Monolithic catalysts have recently attracted much attention owing to their advantages including easy separation and recovery, sufficient exposure of active sites, enhanced heat transfer and mass transfer efficiency. We have demonstrated the excellent catalytic performance of the binary (Cu<sub>0.50</sub>Co<sub>0.50</sub>)<sub>2</sub>Al-Cat powdered catalyst; in this part, we further fabricated the binary monolithic Cu–Co film catalyst obtained from *in situ* growth of the CuCoAl-LDH precursor on aluminum substrates. For the LDH film precursor (Fig. 8A), a series of reflections are observed at  $2\theta$  of 11.6°, 34.9°, 60.1° and 61.4°, which can be attributed to the (003), (012), (110) and (113) reflections of an LDH phase, respectively. Two strong reflections at 44.5° and 65.2° are due to the (200) and (220) reflections of the Al substrate. The stronger characteristic (012) reflection is indicative of a preferential assembly of LDH crystallites with

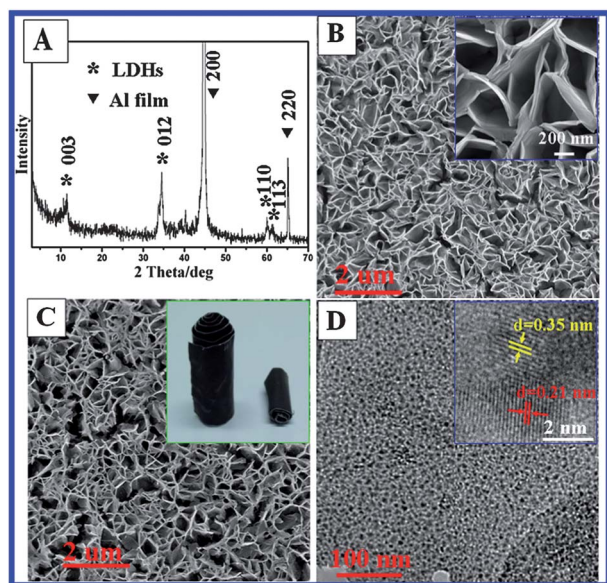


**Fig. 8** (A) XRD pattern of the CuCoAl-LDH film precursor on the Al substrate. SEM images of (B) the CuCoAl-LDH film precursor; the insets show its corresponding enlarged view, (C) the monolithic Cu–Co film catalyst; the insets show the photograph of the rolled Cu–Co film catalyst. (D) TEM images of the monolithic Cu–Co film catalyst; the inset shows the HRTEM lattice fringe image assigned to metal Cu and spinel  $\text{Co}_3\text{O}_4$ , respectively.

their *ab* plane perpendicular to the substrate. The architectural feature of the LDH precursor film was further revealed by SEM (Fig. 8B). It is observed that platelike microcrystals are uniformly distributed with diameter of 1.0–1.5  $\mu\text{m}$  and a thickness of  $\sim 10$  nm, whose *ab*-plane is intercrossing and perpendicular to the substrate. The SEM-EDS analysis of the CuCoAl-LDH film demonstrates that the Cu/Co ratio is 33.5/37.1 (Fig. S7<sup>†</sup>), close to the nominal ratio. The total Cu and Co content on the Al substrate was determined to be 0.363  $\text{mg cm}^{-2}$  by ICP. Calcination and reduction of the LDH film lead to its transformation into the monolithic Cu–Co film catalyst, and the SEM images of the resulting product (Fig. 8C) show that it inherits the original flake morphology of the LDH precursor with a little shrink in the microcrystal size. The TEM images (Fig. 8D) further reveal that high-density Cu nanoparticles (small dark dots) with a diameter of  $\sim 5$  nm were homogeneously dispersed throughout the matrix. Both the metal Cu and the spinel  $\text{Co}_3\text{O}_4$  with lattice spacings of 0.21 nm and 0.35 nm were also identified in the HRTEM image (Fig. 8D, inset), respectively. Therefore, the monolithic Cu–Co film catalyst was obtained *via* a calcination–reduction treatment of the CuCoAl-LDH film precursor.

The catalytic behavior of the as-synthesized Cu–Co film catalyst was evaluated (Fig. 9). For the freshly prepared Cu–Co film catalyst, the catalytic activity was further enhanced with a hydrolysis completion time of 3.0 min compared with the corresponding powdered catalyst ( $\text{Cu}_{0.50}\text{Co}_{0.50}$ )<sub>2</sub>Al-Cat in the same total Cu and Co content. In general, powdered catalysts are subjected to the agglomeration of nanoparticles during the reaction. The advantages of the highly dispersed Cu–Co film catalyst, which facilitates a sufficient exposure of active sites

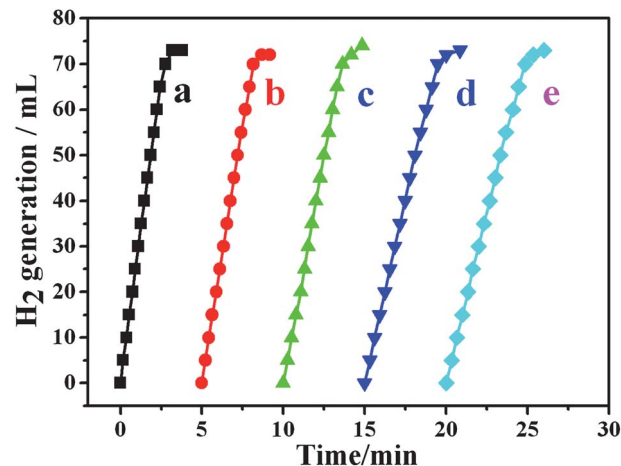


**Fig. 9** Hydrogen evolution from the hydrolysis of ammonia borane catalyzed by the as-prepared monolithic Cu–Co film catalyst (film area: 30  $\text{cm}^2$ ;  $[\text{AB}] = 50$  mM,  $(\text{Cu} + \text{Co})/\text{AB} = 0.09$ ,  $T = 25 \pm 1$   $^\circ\text{C}$ ). The catalyst was repeatedly used for 5 consecutive cycles from curve a to e.

and decreases the mass transfer resistance for AB hydrolysis, are most probably responsible for the enhanced catalytic performance. In addition, reusability and durability of the catalyst are essential factors to be considered before moving towards applications. An evaluation test was performed to recycle the film catalyst through the following steps: (1) carrying out the hydrolysis reaction with a freshly prepared catalyst film; (2) withdrawing and washing the catalyst film with distilled water and ethanol followed by drying at 60  $^\circ\text{C}$  in a vacuum oven; (3) reusing this catalyst with a newly prepared AB solution. The hydrogen generation volume as a function of time, for a given number of runs, is shown in Fig. 9b–e. It is found that no significant activity loss of the Cu–Co catalyst film was observed in five consecutive cycles, demonstrating sufficient reusability and durability of the film catalyst. The structural and functional superiority of the Cu–Co film catalyst makes it an exciting highly efficient candidate in AB hydrolysis for the hydrogen generation system.

## 4 Conclusion

In summary, binary highly dispersed Cu–Co powdered and monolithic film catalysts were fabricated *via* the LDH precursor approach, which display excellent catalytic behavior towards hydrogen generation from  $\text{NH}_3\text{BH}_3$  decomposition. The catalytic activity is seriously dependent on the relative content of the metal element, and the Cu–Co catalyst with the molar ratio of 1/1 is the most active and even comparable to noble metal catalysts. The structural characterizations (XRD, TPR, TEM) confirm that Cu and Co species in the fresh catalyst exist as an active metal Cu and an inactive spinel ( $\text{Co}_3\text{O}_4$ ) form, respectively. Partial reduction of  $\text{Co}_3\text{O}_4$  to the highly active metal Co phase possibly induced by the Cu nanoparticles occurs during the catalytic reaction confirmed by XPS. The high dispersion of Cu and Co species in the LDH matrix maximizes the synergistic effect of binary components, accounting for the resulting

satisfactory catalytic activity. Moreover, the catalytic performance of the monolithic Cu–Co film catalyst was further improved compared with the powdered catalyst, including higher activity and excellent recyclability. This work offers a feasible and practical route to hydrogen storage and generation for fuel cells.

## Acknowledgements

This work was supported by the 973 Program (Grant no. 2011CBA00504), the National Natural Science Foundation of China (NSFC) and the Program for Changjiang Scholars and Innovative Research Team in University (IRT1205). M. Wei particularly appreciates the financial aid from the China National Funds for Distinguished Young Scientists of the NSFC.

## Notes and references

- 1 Q. Xu and M. J. Chandra, *J. Alloys Compd.*, 2007, **446**, 729.
- 2 C. W. Hamilton, R. T. Baker, A. Staubitze and I. Manners, *Chem. Soc. Rev.*, 2009, **38**, 279.
- 3 C. E. Bunker and M. J. Smith, *J. Mater. Chem.*, 2011, **21**, 12173.
- 4 H. W. Langmi and G. S. McGrady, *Coord. Chem. Rev.*, 2007, **251**, 925.
- 5 C. W. Hamilton, R. T. Baker, A. Staubitze and I. Manners, *Chem. Soc. Rev.*, 2009, **38**, 279.
- 6 A. Gutowska, L. Li, Y. Shin, C. M. Wang, X. S. Li, J. C. Linehan, R. S. Smith, B. D. Kay, B. Schmid, W. Shaw, M. Gutowski and T. Autrey, *Angew. Chem., Int. Ed.*, 2005, **44**, 3578.
- 7 U. B. Demirci and P. Miele, *Energy Environ. Sci.*, 2009, **2**, 627.
- 8 Z. Li, G. Zhu, G. Lu, S. Qiu and X. Yao, *J. Am. Chem. Soc.*, 2010, **132**, 1490.
- 9 Ö. Metin, V. Mazumder, S. Özkar and S. H. Sun, *J. Am. Chem. Soc.*, 2010, **132**, 1468.
- 10 H. L. Jiang and Q. Xu, *Catal. Today*, 2011, **170**, 56.
- 11 B. Peng and J. Chen, *Environ. Sci. Technol.*, 2008, **1**, 479.
- 12 T. M. Douglas, A. B. Chaplin, A. S. Weller, X. Yang and M. B. Hall, *J. Am. Chem. Soc.*, 2009, **131**, 15440.
- 13 D. W. Himmelberger, C. W. Yoon, M. E. Bluhm, P. J. Carroll and L. G. Sneddon, *J. Am. Chem. Soc.*, 2009, **131**, 14101.
- 14 M. Chandra and Q. Xu, *J. Power Sources*, 2006, **156**, 190.
- 15 F. Durap, M. Zahmakiran and S. Ozkar, *Appl. Catal., A*, 2009, **369**, 53.
- 16 S. B. Kalidindi, J. Joseph and B. R. Jagirdar, *Energy Environ. Sci.*, 2009, **2**, 1274.
- 17 O. Metin, S. Sahin and S. Ozkar, *Int. J. Hydrogen Energy*, 2009, **34**, 6304.
- 18 T. Umegaki, J. M. Yan, X. B. Zhang, H. Shioyama, N. Kuriyama and Q. Xu, *Int. J. Hydrogen Energy*, 2009, **34**, 3816.
- 19 X. J. Yang, F. Y. Cheng, J. Liang, Z. L. Tao and J. Chen, *Int. J. Hydrogen Energy*, 2009, **34**, 8785.
- 20 C. F. Yao, L. Zhuang, Y. L. Cao, X. P. Ai and H. X. Yang, *Int. J. Hydrogen Energy*, 2008, **33**, 2462.
- 21 Q. Xu and M. Chandra, *J. Power Sources*, 2006, **163**, 364.
- 22 M. Zahmakiran and S. Ozkar, *Appl. Catal., B*, 2009, **89**, 104.
- 23 S. Karahan, M. Zahmakiran and S. Özkar, *Chem. Commun.*, 2012, **48**, 1180.
- 24 S. Basu, A. Brockman, P. Gagare, Y. Zheng, P. V. Ramachandran, W. N. Delgass and J. P. Gore, *J. Power Sources*, 2009, **188**, 238.
- 25 F. Durap, M. Zahmakiran and S. Ökar, *Int. J. Hydrogen Energy*, 2009, **34**, 7223.
- 26 M. Chandra and Q. Xu, *J. Power Sources*, 2006, **156**, 190.
- 27 N. Mohajeri, A. T-Raissi and O. Adebisi, *J. Power Sources*, 2007, **167**, 482.
- 28 N. Patel, R. Fernandes, G. Guella and A. Miotello, *Appl. Catal., B*, 2010, **95**, 137.
- 29 J. M. Yan, X. B. Zhang, S. Han, H. Shioyama and Q. Xu, *Angew. Chem., Int. Ed.*, 2008, **47**, 2287.
- 30 X. H. Zhou, Z. X. Chen, D. H. Yan and H. B. Lu, *J. Mater. Chem.*, 2012, **22**, 13506.
- 31 D. H. Sun, V. Mazumder, Ö. Metin and S. H. Sun, *ACS Nano*, 2011, **5**, 6458.
- 32 J. Wang, Y. L. Qin, X. Liu and X. B. Zhang, *J. Mater. Chem.*, 2012, **22**, 12468.
- 33 N. Patel, R. Fernandes, G. Guella, A. Kal, A. Miotello, B. Patton and C. Zanchetta, *J. Phys. Chem. C*, 2008, **112**, 6968.
- 34 J. A. Gursky, S. D. Blough, C. Luna, C. Gomez, A. N. Luevano and E. A. Gardner, *J. Am. Chem. Soc.*, 2006, **128**, 8376.
- 35 G. R. Williams and D. O'Hare, *J. Mater. Chem.*, 2006, **16**, 3065.
- 36 A. M. Fogg, A. L. Rohl, G. M. Parkinson and D. O'Hare, *Chem. Mater.*, 1999, **11**, 1194.
- 37 L. Li, Y. Feng, Y. Li, W. Zhao and J. Shi, *Angew. Chem., Int. Ed.*, 2009, **48**, 5888.
- 38 H. C. Liu and E. Z. Min, *Green Chem.*, 2006, **8**, 657.
- 39 K. H. Goh, T. T. Lim and Z. L. Dong, *Water Res.*, 2008, **42**, 1343.
- 40 C. Li, L. Y. Wang, M. Wei, D. G. Evans and X. Duan, *J. Mater. Chem.*, 2008, **18**, 2666.
- 41 S. He, S. T. Zhang, J. Lu, Y. F. Zhao, J. Ma, M. Wei, D. G. Evans and X. Duan, *Chem. Commun.*, 2011, **47**, 10797.
- 42 M. Q. Zhao, Q. Zhang, J. Q. Huang and F. Wei, *Adv. Funct. Mater.*, 2012, **22**, 675.
- 43 S. Velu, K. Suzuki, M. P. Kapoor, S. Tomura, F. Ohashi and T. Osaki, *Chem. Mater.*, 2000, **12**, 719.
- 44 G. Fierro, M. L. Jacono, M. Inversi, R. Dragone and P. Porta, *Top. Catal.*, 2000, **10**, 39.
- 45 J. Agrell, H. Birgersson, M. Boutonnet, I. Melián-Cabrera, R. M. Navarro and J. L. G. Fierro, *J. Catal.*, 2003, **219**, 389.
- 46 Z. L. Wang and X. Y. Kong, *J. Phys. Chem. B*, 2003, **107**, 8275.
- 47 Y. Yamada, K. Yano and Q. Xu, *J. Phys. Chem. C*, 2010, **114**, 16456.